# Microstructure and defect sensitivities in the very high-cycle fatigue response of Laser Powder Bed Fused Ti–6Al–4V

Grégoire Brot [a,b,*], Imade Koutiri [b], Vincent Bonnand [a], Véronique Favier [b], Corinne Dupuy [b], Nicolas Ranc [b], Patrick Aimedieu [c], Fabien Lefebvre [d], Robin Hauteville [d]

[a] DMAS, ONERA, Université Paris Saclay, 29 Avenue de la Division Leclerc, Châtillon, France
[b] PIMM, Arts et Metiers Institute of Technology, CNRS, Cnam, HESAM University, 151 Boulevard de l'Hopital, Paris, France
[c] Navier, Ecole des Ponts, Univ Gustave Eiffel, CNRS, Marne-la-Vallée, France
[d] CETIM, 52 Avenue Félix Louat, Senlis, France

## ABSTRACT

This work aims to analyze the sensitivity of the very high-cycle fatigue behavior of LPBF-Ti-6Al-4V to microstructure and porosity variations. To do so ultrasonic fatigue testing is performed on five grades of LPBF-Ti-6Al-4V. These grades were generated using different LPBF process parameters and different thermal post-treatments allowing to separately investigate the sensitivity to microstructure and porosity variations. It was found that both material features highly influenced the VHCF properties of LPBF-Ti-6Al-4V revealing the sensitivity to these features. Furthermore, the largest defect (pore or grain) controls fatigue crack initiation.

## 1. Introduction

Ti–6Al–4V is the most used titanium alloy with a wide range of applications thanks, among others, to its high strength to weight ratio or fatigue strength. Additive manufacturing (AM) of this alloy using Laser Powder Bed Fusion (LPBF) is a relatively mature technology. Ti–6Al–4V is indeed one of the most studied alloy in additive manufacturing with more than 1800 research articles on ScienceDirect website mentioning "Ti–6Al–4V" and "LPBF" (or "SLM"). Printed pieces have now porosity usually lower than 0.5% [1,2]. Nevertheless, significant dispersion of pore size are observed within and in between LPBF printing batches [3] and pore size strongly affects high and very high cycle fatigue (HCF, VHCF) strength [3–5]. Furthermore, Spears and Gold [6] identified 50 key process parameters in LPBF and many of them can affect the fatigue strength through porosity or microstructural changes. In this context, parameter optimization in regards to fatigue strength is a huge challenge because of long testing time. This duration can be significantly reduced using ultrasonic fatigue machines that allow fatigue testing at 20 kHz. However, the sensitivity of VHCF properties in 20 kHz fatigue testing to the specific microstructure and porosity of AM materials was not studied yet. Therefore, in this work ultrasonic fatigue is used to study the VHCF properties of LPBF parts. Some of the tested parts were printed using manufacturing parameters that generate a minimal porosity and some were printed using parameters that lead to an higher porosity. In addition to their different porosity levels, tested parts had distinct microstructures generated by different post heat-treatments.

During LPBF process the small meltpool size and the relatively high scanning speed of the laser lead to very high cooling rates from $10^3$ to $10^8$ K/s [7]. As the result, the microstructure of as-built Ti–6Al–4V is an ultrafine lamellar one. Ti–6Al–4V is an $\alpha + \beta$ titanium alloy at room temperature. Above $\beta$-transus temperature $T_\beta \approx 1000°C$, it is fully composed of $\beta$ phase. According to X-ray diffraction (XRD) analysis from [2,8,9], the as-built microstructure is only composed of martensitic $\alpha'$ phase when using standard process parameters. Indeed, martensitic $\alpha'$ can be decomposed into $\alpha + \beta$ using specific process parameter that maintain an higher temperature of the printed part during process [10,11]. During printing process, each point of LPBF part is subjected to successive heating and cooling phases as layers are deposited and laser-scanned. Yang et al. [12] studied this specific thermal history and its effects on the formation of $\alpha'$ phase. As-built microstructure present a hierarchical structure composed of four types of martensite $\alpha'$-lamellae with a decreasing size. Primary lamellae are the largest ones with a width from 1 to 3 μm. Moreover, two main types of porosity can be found in LPBF parts: lack of fusion pore and spherical gas pore. The different mechanisms causing the formation of these pores are detailed in [13]. The first ones have an irregular shape,

are often filled with unmelted powder particle and tend to be larger in the plane perpendicular to building direction. They can be formed when the laser bring insufficient energy to the powder. The second ones have a regular and spherical shape. Spherical gas pore can be subdivided between blowhole pore and keyhole pore. Blowhole pores are gas bubble trapped during solidification with a maximal size of 30 to 50 μm. Keyhole pores are large and spherical ones that are formed during the collapse of the vapor capillary that appear when the welding mode is a keyhole mode [13]. This welding mode appears with high laser intensity.

Furthermore, as-built LPBF parts retain high residual stresses also related to the high cooling rate and the layer by layer heating process. Leuders et al. [14] found out using XRD that these stresses are tensile ones at the surface with a magnitude from several hundred MPa in the as-built state. According to Leuders et al. residual stresses presented a rather low influence on monotonic or fatigue strength. Residual stresses are negligible when parts are treated at 800°C for 2h [14]. Similar stress relieving results were obtained by Syed et al. [15] using the contour method. They found out a 90% reduction of stresses when treated at 680°C for 3 h. It is therefore relevant to study the thermal post-treatment for this material. Annealing treatments at sub β-transus temperature have two main effects on LPBF–Ti–6AL–4V microstructure. The first one is the decomposition of the metastable phase α' into α + β phases. Kaschel et al. [16] showed using in-situ high temperature XRD that the decomposition appeared above 500°C and is fully completed when treated at 750°C. According to Etesami et al. [17] α' martensite is fully decomposed after 2 h at 900°C. When treated at 900°C, β phase is formed as both particles and rod-shaped. When treated at 611°C β phase precipitated mostly into fine particles. The second main effect of sub β-transus annealing treatment is the coarsening of α/α' lamellae. In these microstructures each α/α' lamellae correspond to a crystallographic grain. Vrancken et al. [9] showed that temperature has a greater impact on lamellae coarsening than resident time or cooling rate for treatment below β-transus. Width of lamellae goes from 1.22 to 2.23 μm for treatment at 850 to 940°C. In the case of super transus-β treatment, primary β grains become equiaxed as reported in [9,18]. For sufficiently low cooling rate, colonies of α + β lamellae are formed out of high temperature β grains. Ter Haar et al. [19] showed using electron backscatter diffraction (EBSD) that each colony of α + β lamellae is a grain as it has a unique crystallographic orientation.

The specific microstructure of LPBF–Ti–6Al–4V affects its mechanical properties. Several authors [9,14,17,20,21] studied the effect of heat-treatment on its mechanical properties. As-built LPBF–Ti–6Al–4V shows an higher tensile strength but a lower fracture elongation compared to conventionally manufactured one [2]. With an increasing temperature of treatment, yield strength tends to decrease while fracture elongation increases. According to Etesami et al. [17], ductility increase and yield strength decrease are related to the martensite decomposition during which volume fraction of the more ductile β phase increases while the one of brittle α' phase decreases. Zhang et al. [22] estimated a β volume fraction of 3% (resp. 9%) after treatment at 730°C (resp. 900°C). For treatment temperatures higher than 800°C, once α'martensite is fully decomposed, ductility increase is related to the growth of α laths [17].

Concerning fatigue, Bathias and Paris [23] showed that some parts in the aeronautical industry, the main application domain of Ti–6Al–4V, are loaded in high and very-high cycle fatigue. It is therefore of a great interest to study the HCF and VHCF behavior of this alloy. According to the review from Li et al. [24], process-induced porosity and surface quality appear to have the greatest effect on fatigue strength of LPBF–Ti–6Al–4V. Kasperovich and Hausmann [1] found a significant fatigue life increase between as-built and machined specimens but a similar fatigue life between machined specimens and specimens that were both heat-treated and machined. However, thermal treatments also impact fatigue strength [24]. For comparison purpose, we plotted in Fig. 1 the effect of thermal post-treatment on the

HCF performance of machined or polished LPBF–Ti–6Al–4V based on testing results collected in [1,25–32]. The results for forged Ti–6Al–4V with a duplex microstructure were also plotted. These results show a high scatter within each study and in between different studies. For example, scatter, evaluated as the standard deviation associated with a log-normal distribution of stresses at $10^7$ cycles, is 30 MPa (resp. 50 MPa) for the "Stress-relieving" (resp. "Sub-transus annealing") series of data in Fig. 1. Le et al. [3] explained this scatter because of the different sizes and types of pores acting as fatigue crack initiation sites. Scatter is reduced when using hot isostatic pressing (HIP) treatment as it allows to close most of the process-induced pores, leading to superior fatigue properties [1,25] (Fig. 1). Several authors used the Kitagawa–Takahashi (KT) diagram, originally proposed in [4], in order to analyze the effect of the size of pores on the fatigue limit of LPBF–Ti–6Al–4V. Le et al. [3] and Hu et al. [33] proposed a generalized KT diagram including fatigue life beside applied stress and size of defects. Using this, Le et al. [3] showed that crack initiation on internal pores leads to a significantly higher fatigue life than initiation on surface pores with the same size and tested under the same stress amplitude. Furthermore, this generalized diagram did not discriminate sample printed in different building directions meaning that the anisotropy of fatigue strength is only related to the apparent size of pores relative to the loading direction. As both the type and location of pore influence fatigue life, Le et al. [3] proposed a ranking of critical defect types. The most harmful ones are surface lack of fusion followed by internal lack of fusion, surface gas pore and internal gas pore. The effect of sub-β-transus treatment on fatigue performance is complex. Indeed, grain coarsening and yield strength reduction should reduce fatigue strength while residual stress relieving and ductility increase tend to increase it. Furthermore, super-β-transus treatment or super-β-transus HIP lead to reduced fatigue strength related to an excessive grain growth and reduced yield strength [25].

Results presented in Fig. 1 highlight the fact that many process of post-process parameter can influence the fatigue strength of this material. Studying the effect of each parameter requires long testing campaign unless rapid testing method are used. LPBF–Ti–6Al–4V was studied in VHCF regime using ultrasonic fatigue. Wycisk et al. [30] and Günther et al. [27] performed both high and very-high cycle fatigue tests up to $10^9$ cycles. In both study, fatigue crack initiated always on pores for non-HIPed specimens showing the first-order role of defect in the VHCF regime [27,30]. Fatigue strength is still decreasing in the VHCF regime without showing any asymptotic behavior whereas results for forged material are clearly asymptotic for fatigue life higher than $10^6$ cycles. In these studies [27,30], both conventional and ultrasonic fatigue tests were performed and no significant effect of the testing frequency was noticed by the authors. In the VHCF regime, crack initiation of almost all specimens is internal whereas most of it were at the surface in the HCF regime. For HIPed specimens in [27], fatigue crack initiation is located on facets of α phase without any visible pore. More recently, Chi et al. [34] studied VHCF crack initiation using ultrasonic fatigue under two stress ratios ($R = -1$ or $R = 0.5$). For $R = -1$, fatigue life diagram is a multi-stage one as defined in [35]. Indeed, cracks initiated on surface in the HCF regime whereas they initiated in the bulk in the VHCF regime. In the case of internal crack initiation, only specimens tested with a load ratio of $R = -1$ presented near crack origin a nanograin layer, visible as a rough area on fractography.

Although extremely low porosity levels are not guaranteed, some LPBF–Ti–6Al–4V parts are almost fully dense. As a results, fatigue crack can initiate on microstructural feature on non-HIPed LPBF–Ti–6Al–4V specimens as observed by Le at al. [3] on one specimen or by Pessard et al. [36] when highly-stressed volume is low. Furthermore, Moran et al. [21] observed both porosity-induced and microstructure-induced fatigue crack initiation on three batches of HIP treated LPBF–Ti–6Al–4V whatever the porosity level prior to HIP treatment. With the increasing experience of LPBF machine manufacturers and users, extremely low porosity levels should become more common. Therefore, transition
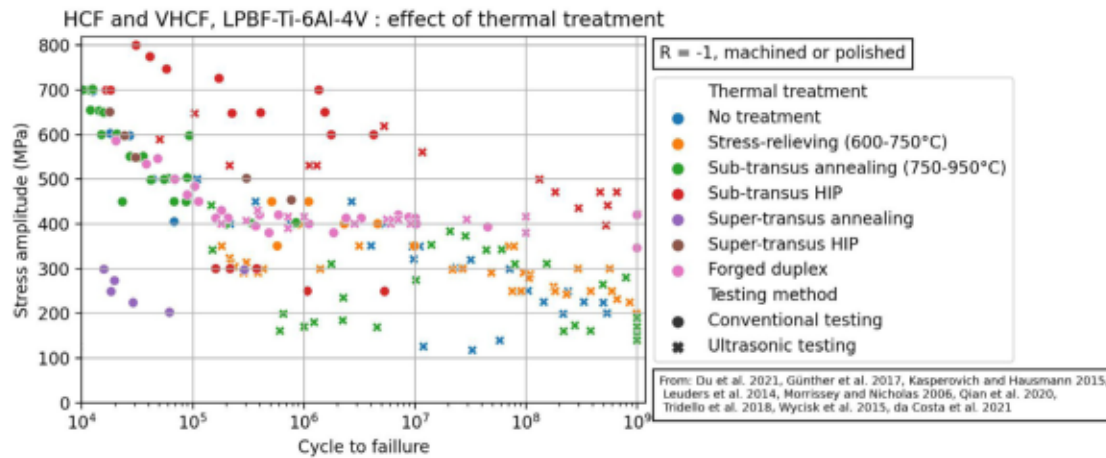
**Fig. 1.** High and very high cycle fatigue results showing the effect of thermal treatment on the fatigue strength of LPBF–Ti–6Al–4V. Specimens are either machined or polished. For all, load ratio is $R = -1$. Results collected from [1,25–31].

between porosity-induced and microstructure-induced fatigue failure of LPBF–Ti–6Al–4V is of a great interest.

The present works aims to investigate the effect of microstructure and porosity on the VHCF behavior of LPBF–Ti–6Al–4V using ultrasonic fatigue testing. The properties of five grades of LPBF–Ti–6Al–4V that have different porosity levels or microstructures were studied. This allows separately studying the effect of these two material features as both are known to affect fatigue properties. Prior to fatigue testing, the five materials grades were characterized using microtomography, EBSD, electron microscopy and monotonic tensile testing. Following fatigue testing, fractographic analysis were performed.

## 2. Methods

### 2.1. Sample processing and microscopic analysis

Specimen preparation aims to produce five grades of LPBF–Ti–6Al–4V that have different microstructures and porosity levels. Three grades should have the same porosity level but different microstructures and three grades should have different porosities but the same microstructure. The different processing routes used to get these grades are presented in Fig. 2. First, two porosity levels, noted $P_1$ and $P_2$, are generated during LPBF process with different laser scan strategies. Then, the different microstructures are generated with different thermal treatments. The third porosity level, noted $P_0$, is obtained using an Hot Isostatic Pressing (HIP) treatment.

All specimens were vertically printed as round bars using a SLM125 machine (SLM Solutions GmbH). Powder used is a Ti–6Al–4V from 3D SYSTEMS (LaserForm® Ti Gr5 (A)). 10% (resp. 90%) of powder particle size is lower than 20 µm (resp. 57 µm). LPBF process was done using a laser power of 275 W, an hatch distance of 120 µm, a scan speed of 1100 mm/s and a layer thickness of 30 µm. Building plate temperature was 150°C. During printing process, the "Sky-Writing" mode was deactivated. This mode enables to move the scanner at full speed all along the scanning vector length while without it, the scanner accelerates and decelerates at each vector extremity with the laser turned on. Therefore, the laser brings more energy to the powder at those locations and the high energy intensity leads to likelier formation of keyhole pores. Fig. 3, present the two scanning strategy used. Zones in the neighbor of scanning vector extremities where formation of keyhole pores is likelier are highlighted on Fig. 3. In order to get parts with a porosity $P_2 \approx 1\%$ and a quasi-homogeneous distribution of pores in the bulk, a chessboard scanning strategy and an inter-layer rotation of 15° are used. Width of chessboard pattern is set to 4.7 mm. Build processor generates the chessboard pattern on Fig. 3.b. in which some chessboard squares are merged to avoid too short scanning vectors. Part

with a porosity $P_1$ are processed with laser track going through the part width and have in their bulk a porosity close to 0.001% (Fig. 3.a). Many large pores are produced at the edges of parts but these are removed during post-processing. Specimens were fabricated within five printing batches. Cylinders with a length of 100 mm and a diameter of 13 mm were printed for tensile testing. For ultrasonic fatigue testing, printed cylinders are 80 mm long with a 13 mm diameter.

All samples are then heat-treated (Fig. 2 and Table 1). Parts with a porosity $P_2$ were treated at 920°C for 2 h followed by furnace cooling. Parts printed with a porosity $P_1$ were divided into four groups randomly distributed within all printing batches. The first group was treated at 650°C for 3 h followed by air cooling, the second one is treated at 920°C for 2 h followed by furnace cooling, the third one is treated at 1020°C for 2 h followed by furnace cooling and the forth group was HIPed at 920°C at a pressure of 2000 bar for 2 h. This pressure level was chosen because some rare pores were still detected during Backscatter electron (BSE) observations of cubic samples treated with a 1000 bar HIP process with the same duration and temperature. During furnace cooling and HIP cooling, average cooling rate from high temperature to 500°C was close to 0.04°C/s. The five material grades are noted in the following according to their porosity level and treatment temperature: $P_0\_920°C$, $P_1\_650°C$, $P_1\_920°C$, $P_1\_1020°C$ and $P_2\_920°C$. Specimens were then machined to their final geometry presented in Fig. 4. Then, VHCF specimens were polished with paper grit up to 4000. Some cubic samples were also processed for microstructural analysis. BSE microscopy and EBSD analysis were performed with a TESCAN MIRA microscope. EBSD view field was $700 \times 700$ µm with a spatial resolution of 500 nm.

Porosity of some specimens was analyzed using microtomography at the Navier laboratory in France. The microtomograph was an Ultratom made by RX Solutions, equipped with a L10801 X-ray source (max 230 kV) and a Varex 4343 DX-I imager ($3052 \times 3052$ active pixels, pixel size is 139 microns). Acceleration voltage was set to 140 kV, current was 28 µA. Imager frame rate and averaging were respectively 1 and 8 and 2368 projections were acquired per sample. Samples were scanned with a voxel size of $4 \times 4 \times 4$ µm³. Successive sample scans were automatized by placing samples in column in the tomograph and performing scans automatically one after another. Sample positioning was fixed to avoid motion during scan, by using long carbon fiber stems, which were attached to the column of samples from top to bottom.

As the size of pores and voxel were close, a simple binarization of tomographic data was not suited to estimate porosity and the size of pores. Therefore, two threshold grey levels were defined for each scanned sample: $I_{metal}$ and $I_{void}$. These thresholds were defined using
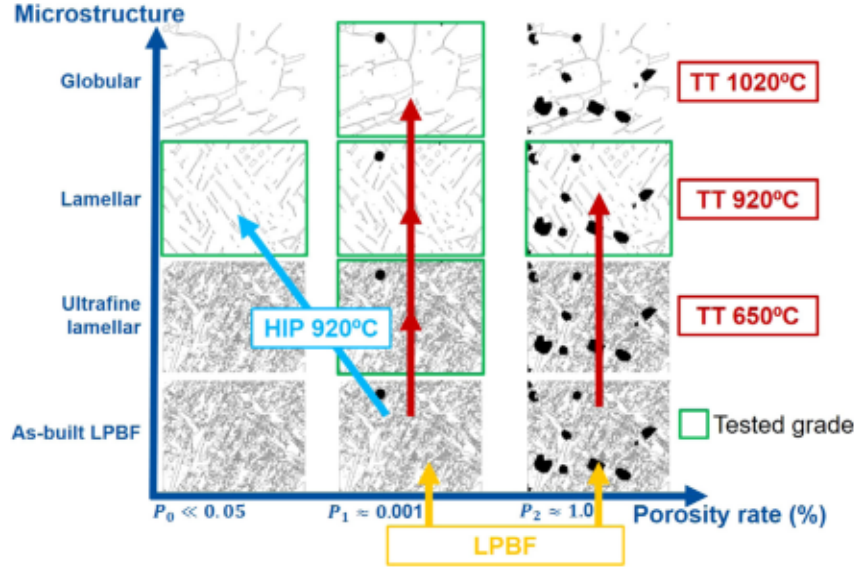
**Fig. 2.** Different processing routes used to get specimen with different porosity levels or microstructures. HIP stands for hot isostatic pressing treatment. TT stands for thermal treatment.
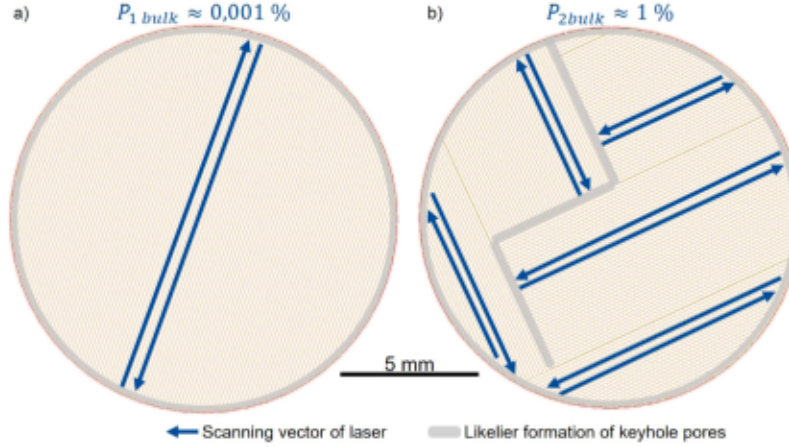


**Fig. 3.** Examples of laser tracks within one scanned layer during LPBF processing of test specimens. (a) Tracks are going through the part leading to porosity $P_1$ in the bulk of parts. (b) Chessboard pattern leading to a porosity $P_2$ in the bulk of parts if "Sky-Writing" mode is deactivated. Inter-layer rotation or scanning pattern is 15°.

**Table 1**
Description of the different thermal post-treatments used to generate the different material grades.

| Grade | Temperature of treatment | Duration | Cooling type | Atmosphere |
|---|---|---|---|---|
| $P_1\_650°C$ | 650°C | 3 h | Air cooling | Argon |
| $P_{1,2}\_920°C$ | 920°C | 2 h | Furnace cooling | Argon |
| $P_1\_1020°C$ | 1020°C | 2 h | Furnace cooling | Argon |
| $P_0\_920°C$ | 920°C | 2 h | Furnace cooling | HIP 2000 bar of argon |

grey level profile across pores. When $I_{voxel_i} \geq I_{metal}$, $voxel_i$ was considered as only composed of metal. When $I_{voxel_i} \leq I_{void}$, $voxel_i$ was considered as only composed of void. For $I_{void} \leq I_{voxel_i} \leq I_{metal}$, $voxel_i$ was considered as partially composed of metal and void fraction was estimated to vary linearly between 1 for $I_{void}$ and 0 for $I_{metal}$. The volume of each pore was obtained by summing each voxel volume times their void fraction. For each pore, equivalent size was calculated as $\sqrt[3]{Volume}$. Pore volume relative error was estimated as:

$$\frac{\sigma(Volume)}{Volume} = \frac{1}{\sqrt{N}} \frac{\sigma(I_{scan})}{I_{metal} - \bar{I}} \quad , \tag{1}$$

where $\sigma(I_{scan})$ is the standard deviation of grey levels in a fully dense region of the scan, $N$ is the number of voxels describing the considered pore and $\bar{I}$ is the mean grey level within the pore. Pore size error was estimated to correspond at maximum to 10% when their volume was greater than 15 voxels ($\sqrt[3]{Volume} \approx 10$ μm). Only pores larger than 15 voxels were considered during data processing. Ratio of porosity was estimated by considering only those pores. This was done to avoid counting noisy isolated voxels as void. Similarly to $\sqrt{Area_{eff}}$ method [5], data processing considered group of pores separated from a distance lower than the size of the smallest pore as one unique pore. Their size was defined from the smallest convex volume that surround all pores of the group. To study the distribution of large pores, block maxima strategy as defined in [33] was used. Scanned volume was divided into 60 sub-volumes. For each sub-volume, the size of the largest pore which centroid is in the sub-volume was collected.
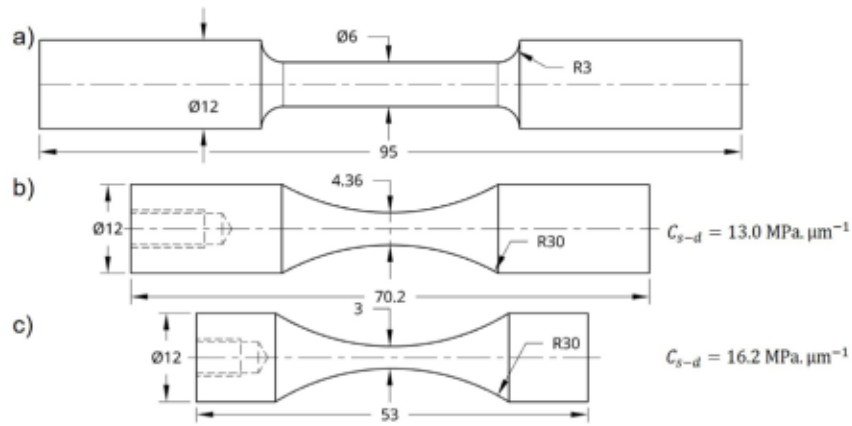
**Fig. 4.** Geometry of specimen used for: (a) tensile testing, (b) for ultrasonic fatigue with a displacement–stress factor of 13 MPa/µm and (c) for ultrasonic fatigue with a high factor of 16.2 MPa/µm (in mm).

**Table 2**
Results of microtomographic analysis of porosity. Two specimens from each material grade excepted $P_2$_920°C were scanned.

| Grade | $P_0$_920°C | $P_1$_1020°C | $P_1$_650°C | $P_1$_920°C | $P_2$_920°C |
|---|---|---|---|---|---|
| Ratio of porosity (ppm) | < 1 | 2 ± 0.2 | 3 ± 0.1 | 11 ± 0.4 | 10713 ± 20 |
| Largest pore (µm) | < 10 | 36 | 51 | 44 | 260 |
| Pore > 10 µm density (mm$^{-3}$) | 0.0 | 0.7 | 0.6 | 2.2 | 117.3 |
| Ratio of porosity (ppm) | < 1 | 2 ± 0.1 | 2 ± 0.1 | 3 ± 0.2 | |
| Largest pore (µm) | < 10 | 35 | 24 | 33 | |
| Pore > 10 µm density (mm$^{-3}$) | 0.0 | 0.4 | 0.7 | 0.6 | |

### 2.2. Tensile and very high cycle fatigue testing

All mechanical tests were performed at room temperature. For each material grade, one specimen was used for tensile testing. Specimen geometry is presented in Fig. 4.a. Tests were done on a servo-hydraulic machine (MTS model 322.21) with a maximal load of 100 kN controlled using TestSuite Multipurpose Elite software. Tensile testing was a two imposed strain rates test followed by a relaxation step. This was done to evaluate the early plastic behavior and to get some insights on the strain rate sensitivity and the viscous behavior of the different material grades. Strain rate was $10^{-2}$ s$^{-1}$ until strain reached 2% then strain rate was suddenly changed to $10^{-3}$ s$^{-1}$ until strain reached 4%, strain rate was then back to $10^{-2}$ s$^{-1}$ until 5%. This last strain was then maintain for 5 min for the relaxation test. Vickers microhardness test were also performed on each grade using a Clemex CMT.HD.

For each material grades, seven to ten fatigue specimens were tested with an ultrasonic fatigue machine. During testing, the machine imposes a sinusoidal displacement at 20 kHz to the specimen. This one vibrates in its first longitudinal eigenmode corresponding to a load ratio $R = -1$. Using modal finite element analysis, specimen were design so that this mode is close to the working frequency of the machine (Fig. 4.b–c). Material behavior was supposed to be linear elastic meaning that the stress amplitude at the center of the specimen is linear with the imposed displacement amplitude. The stress–displacement factor was determined using an harmonic analysis at the working frequency by taking the mean stress amplitude over the central section for an imposed displacement amplitude (Fig. 5). See [37] for more details on the designing step. The design of all specimens except $P_0$_920°C ones is the one in Fig. 4.b associated with a factor $C_{s-d}$ of 13 MPa/µm (Fig. 5). Due to ultrasonic machine limitations, $P_0$_920°C grade which has a higher fatigue strength could not be tested with the geometry on Fig. 4.b. Design of $P_0$_920°C specimens is the one in (Fig. 4.c) so that the stress–displacement factor $C_{s-d}$ is 16.2 MPa/µm. Consequently the highly loaded volume of geometry Fig. 4.c is $V_{0.9max} = 32$ mm$^3$, and the one of Fig. 4.b is $V_{0.9max} = 78$ mm$^3$.

Tests were performed with a homemade machine, which is based on a piezo-electric converter 2000 Series Model CR-20 from Branson™,

see [37] for further details on the testing setup. During fatigue test, displacement amplitude at the free end of specimen was measured using a HSV 2001 laser vibrometer. The stabilized temperature of the specimens did not exceed 40°C thanks to a forced convection cooling system. When a sufficiently large fatigue crack appears in the specimen, the ultrasonic machine stops due to the induced frequency drop. Stress amplitude levels were chosen in order to get a stress to number of cycles to failure (SN) curve near $10^7 - 10^9$ cycles. To determine the corresponding stress level, the first specimen of each material grade was tested with a Locati procedure in which loading steps lasted $10^7$ cycles and stress was increased by 10 MPa between two steps until specimen failed. For the other specimens used to get a SN curve, testing was done at a constant stress amplitude until failure. Test was stopped if it reaches $10^9$ cycles. Specimens that failed were then cooled in liquid nitrogen and broken. Fractography was systematically done using both optical microscopy and scanning electron microscopy (SEM). During fractographic analysis, the size of critical pore was determined using $\sqrt{Area_{eff}}$ method which is based on the projected area of the defect in the plan perpendicular to loading direction [5,38]. Defects were considered as internal ones if the distance between surface and crack initiation $d_{surface}$ was higher than the defect size $\sqrt{Area}$. They were considered as sub-surface ones if $\sqrt{Area} > d_{surface}$. For these ones, the effective area $\sqrt{Area_{eff}}$ which includes the defect and the ligament between defect and surface was considered.

## 3. Results

### 3.1. Microstructure and porosity analysis

Fig. 6 presents BackScatter Electron (BSE) micrographs of the studied microstructures. Microstructure after the 650°C stress relieving treatment is visible in Fig. 6.a. The as-built martensite phase $\alpha$' is partially decomposed into $\alpha + \beta$ [39]. Indeed, BSE micrographs show fine and non-continuous $\beta$-phase around $\alpha/\alpha$' phase. Gil et al. [40] studied this decomposition during annealing treatment of forged Ti–6Al–4V. Most of $\alpha$' should be decomposed for treatment at 650°C for 3 h. The
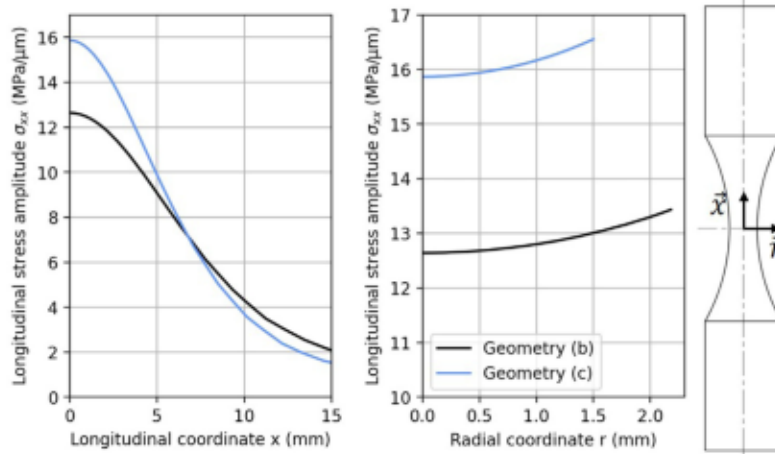
**Fig. 5.** Longitudinal stress amplitude field within ultrasonic fatigue specimens calculated using an harmonic analysis finite element simulation. Imposed displacement is sinusoidal with an amplitude of 1 μm and a frequency of 20 kHz. Geometry (b) and (c) are presented in Fig. 4.
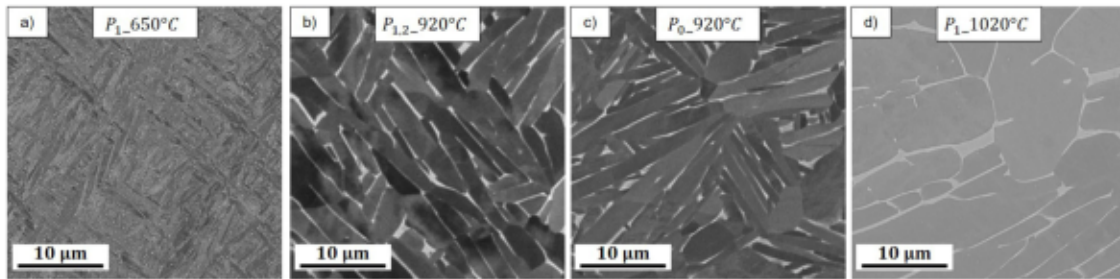


**Fig. 6.** BackScatter Electron micrographs at the same scale of LPBF–Ti–6Al–4V microstructure when, (a) treated at 650°C for 3 h and air cooled, (b) treated at 920°C for 2 h and furnace cooled, (c) HIPed at 920°C and 2000 bar for 2 h, (d) treated at 1020°C for 2 h and furnace cooled. $\beta$-phase is the lighter phase.
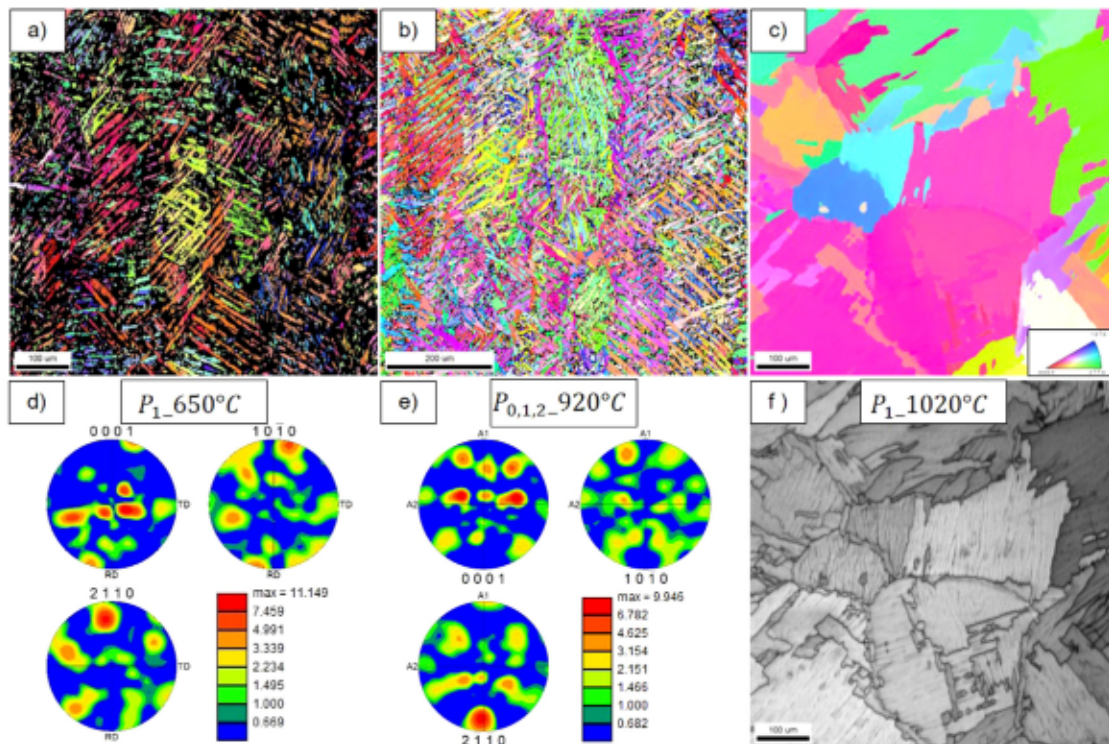


**Fig. 7.** Inverse and direct pole figures from EBSD analysis on Titanium-$\alpha$ phase for samples treated: (a) and (d) at 650°C for 3 h and air cooled, (b) and (e) at 920°C for 2 h and furnace cooled, (c) at 1020°C for 2 h and furnace cooled. (f) Image quality map of the scan (c). Scale of inverse pole figures is the same. Building direction during LPBF process is vertical on inverse pole figures.
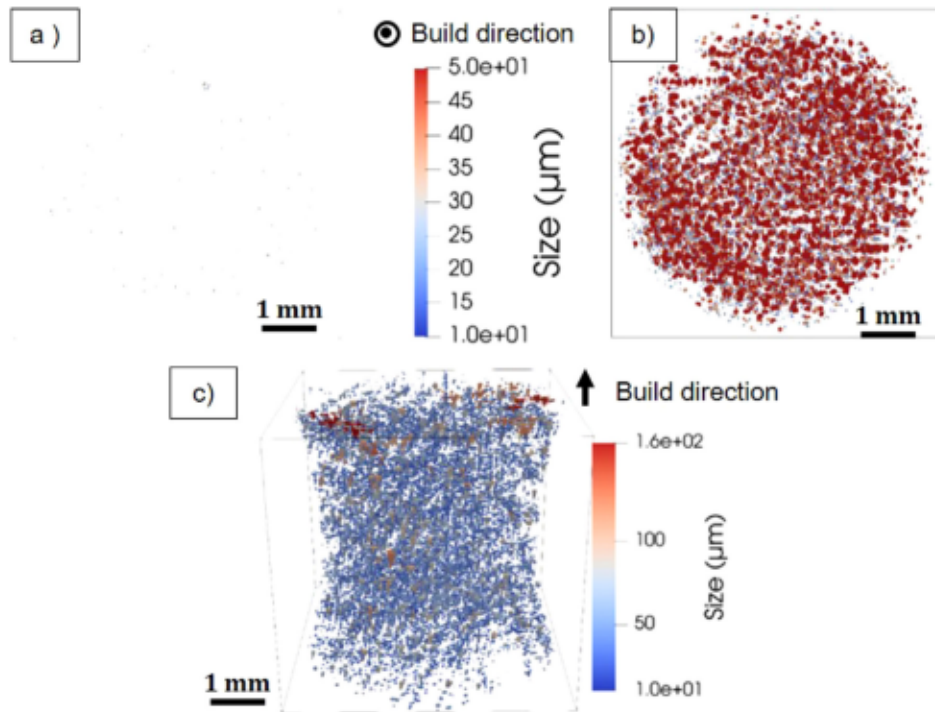
**Fig. 8.** (a) and (b) 2d projections in the plane perpendicular to the building direction of pores detected by microtomography in which scan height was 10.5 mm: (a) a $P_1\_920°C$ scanned specimen, (b) a $P_2\_920°C$ scanned specimen. (c) 3d view of the pores detected in half of whole scan height of $P_2\_920°C$ specimen.
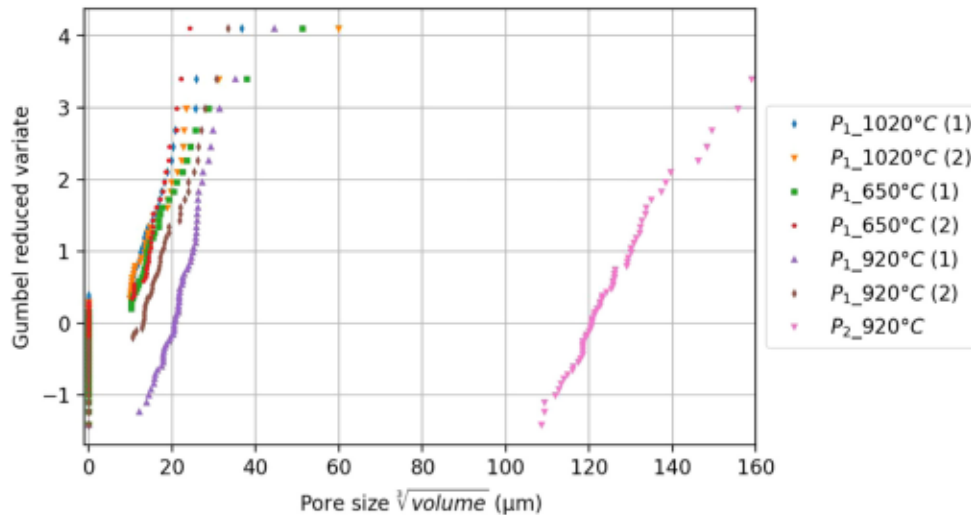


**Fig. 9.** Distribution of largest pores in sub-volumes of tomographic scans.

present microstructure is an ultrafine lamellar one, where the morphology of $\alpha/\alpha'$-lamellae remains close to the one of as-built $\alpha'$-lamellae. The mean width of $\alpha/\alpha'$-lamellae evaluated using the line intercept method on BSE micrographs is 0.4 μm. Proportion of $\beta$-phase was estimated to 3% using image processing of BSE micrographs. Inverse pole figure of EBSD analysis can be seen in Fig. 7.a. Groups of lamellae originated from the same prior $\beta$ grain have a significant texture as discussed in [8]. However, direct pole figure of the $700 \times 700$ μm EBSD scan did not show any significant texture (Fig. 7.d). This microstructure presents therefore a micro-texture but no significant texture at the macroscopic scale.

Microstructure after thermal treatment or HIP at 920°C is lamellar in which $\alpha$-lamellae are 2.2 μm wide. According to [16,17] martensite $\alpha'$ should be fully decomposed into $\alpha + \beta$. The as-built hierarchical structure with primary to quaternary $\alpha'$-lamellae can no longer be

visible as the width of all $\alpha$-lamellae is similar. $\beta$-phase is present as thin bands that are 200 to 800 nm wide. Proportion of $\beta$-phase was estimated to 8% on BSE micrographs. $\beta$-phase is rod-shaped whereas it is present as rod-shaped and particles after sub $\beta$-transus treatment followed by air cooling [17]. Similarly to the first microstructure, groups of textured lamellae are visible in Fig. 7.b without significant texture when analyzing the whole scan (Fig. 7.e). No significant difference between the microstructure obtained after the 920°C treatment or after the HIP treatment is visible. The microstructure after treatment at 1020°C is composed of colony of aligned $\alpha + \beta$ lamellae. The $\alpha$ lamellae have the same crystallographic orientation gathered in a grain (Fig. 7.c). These grains are equiaxed and are 200 μm wide. Mean width of $\alpha$ (resp. $\beta$) lamellae is 5 μm (resp. 0.5 μm). Lamellae of the same colony can be visible on the image quality map of EBSD scan in Fig. 7.f.

**Table 3**
Results of microstructural analysis and mechanical properties for the five studied grades.

| Grade | $P_0\_920°C$ | $P_1\_1020°C$ | $P_1\_650°C$ | $P_1\_920°C$ | $P_2\_920°C$ | Forged bimodal [32] |
|---|---|---|---|---|---|---|
| Width of $\alpha$-lamellae (µm) | $2.2 \pm 0.3$ | $5.0 \pm 1.0$ | $0.4 \pm 0.1$ | $2.2 \pm 0.3$ | $2.2 \pm 0.3$ | |
| Grain width (µm) | $2.2 \pm 0.3$ | $200 \pm 24$ | $0.4 \pm 0.1$ | $2.2 \pm 0.3$ | $2.2 \pm 0.3$ | 15-20 |
| Grain type | $\alpha$-lamellae | $\alpha + \beta$ colony | $\alpha$-lamellae | $\alpha$-lamellae | $\alpha$-lamellae | |
| Present phases | $\alpha + \beta$ | $\alpha + \beta$ | $\alpha'$, $\alpha + \beta$ | $\alpha + \beta$ | $\alpha + \beta$ | $\alpha_p$, $\alpha + \beta$ |
| Porosity (%) | 0.000 | $\approx 0.001$ | $\approx 0.001$ | $\approx 0.001$ | $\approx 1$ | |
| Yield stress 0.2% (MPa) | 1047 | 850 | 1235 | 1024 | 992 | 930 |
| Viscous stress (MPa) | 113 | 132 | | 138 | 150 | |
| Microhardness (HV) | $368 \pm 9$ | $321 \pm 21$ | $374 \pm 6$ | $352 \pm 7$ | $338 \pm 4$ | |

Spatial representations of the pores detected using tomographic data are represented on Fig. 8. Fig. 8.h confirms that the spatial distribution of pores in $P_2\_920°C$ specimens is quasi-homogeneous. Table 2 presents the results of tomographic analysis. Size of pores was calculated as $\sqrt[3]{Volume}$ and only pores for which $\sqrt[3]{Volume} > 10$ µm were considered. In Table 2, estimation of error on the ratio of porosity was based on the error on each pore volume (Eq. (1)). As no pore were detected in $P_0$ samples, error on porosity ratio could not be estimated. Pore size error is less than 1 µm for largest pore in each sample as many voxels describe these pores. Block maxima strategy was used to get the distribution presented in Fig. 9. This corresponds to the distribution of largest pores in sub-volumes represented using Gumbel reduced variate: $y_i = -\ln(-\ln(i/(n + 1)))$ with $n$ the number of sub-volumes and $i$ the $i$th local maximum from the smallest one. The quasi-linear aspect of these curves means that these distributions can be represented using Gumbel distribution. This distribution of the statistic of extreme allows to described the maximum values of a distribution. For more details on block maxima strategy see [33]. In Fig. 9, data with a defect size of 0 µm correspond to sub-volumes in which no pores were detected. Although ratios of porosity of sample printed using $P_1$ parameter are different (Table 2), the size of their largest pore and their Gumbel distribution are similar. Meaning that this porosity level is reproducible and not affected by thermal post-treatment. Moreover, spatial distribution of pores was homogeneous in each scanned sample.

### 3.2. Mechanical properties

Stress–strain curves of the tensile tests are represented in Fig. 10. Table 3 presents for each grade the size of microstructure, the porosity, the yield stress at 0.2% of plastic strain, the viscous stress relaxed during the 5 min relaxation at a strain of 5% and the microhardness. The specimen of $P_1\_650°C$ grade broke outside the gauge of extensometer before relaxation step. Other specimen did not fail during test. The different microstructures strongly affect tensile behavior. Relationship between grain width $d$ and yield stress $\sigma_y$ follows Hall–Petch relationship: $\sigma_y = \sigma_0 + \frac{k}{\sqrt{d}}$ with $\sigma_0 = 830$ MPa and a strengthening coefficient $k = 0.25$ MPa$\sqrt{m}$. Here, $d$ is considered to be the $\alpha$- lamellae width for 650°C and 920°C grades. In the case of $P_1\_1020°C$, $d$ is considered to be the width of $\alpha + \beta$ colony in which $\alpha$-lamellae have the same crystallographic orientation and consequently are not strong barrier to crystallographic slip. Compared to microstructure, porosity has a lower impact on tensile behavior. Yield stress is reduced by 5% (55 MPa) when porosity goes from $P_0 \approx 0\%$ to $P_2 \approx 1\%$. It can be noted that this reduction is not linear with the ratio of porosity. Close values of viscous stress and close stress drop at 2% strain were obtained for the five material grades. This means that the five grades have similar strain-rate sensitivity.

### 3.3. VHCF testing results

Fig. 11 presents the stress amplitude to cycles to failure (SN) curves of the ultrasonic fatigue test results. These ones are presented according to the material grade of specimen and the type of fatigue crack initiation. Among grades with a $P_1$ porosity, $P_1\_920°C$ has the highest fatigue strength and $P_1\_1020°C$ the lowest. Microstructural changes between these two grades lead to a 180 MPa drop in VHCF resistance. The stress relieved $P_1\_650°C$ has a fatigue strength close but lower than $P_1\_920°C$. As expected, fatigue strength decrease with porosity level for a constant grain size. Porosity in $P_2\_920°C$ specimens lead to a 260 MPa drop in fatigue strength at $10^7$ cycles as compared to $P_0\_920°C$. SN curves for $P_1\_920°C$, $P_1\_650°C$ and $P_2\_920°C$ grades do not show any asymptotic behavior whereas the other does. These correspond to grades for which initiation was porosity-induced. In Fig. 11, curves of fitted power law are represented for each grade. SN curves of grades $P_1\_920°C$ and $P_1\_650°C$ present two modes according to the type of pore at initiation. These curves are therefore associated with a large scatter.

The majority of crack initiations were internal. Similarly to the results of Heinz et al. [41] distance between surface and crack initiation $d_{surface}$ is lower than 640 µm for 70% of specimens, which represent half of the section area. However, the amplitude of the longitudinal stress in this zone is only $\approx 5\%$ greater than the amplitude of the stress on the axis of the specimen. Longitudinally along the specimen, maximum distance between crack initiation site and mid-section of sample was 2.7 mm. Within this range, local stress determined using finite element analysis is close ($discrepancy < 10\%$) to the one in longitudinally mid-section. Within all fatigue specimens, three types of fatigue crack initiations were observed: initiation around spherical gas pore (blowhole or keyhole), initiation around lack of fusion pore, initiation region without visible pore (Fig. 12). The most common case is initiation around spherical gas pore. Crack initiated always around pores and without microstructural facets in grades $P_1\_650°C$, $P_1\_920°C$ and $P_2\_920°C$. For these ones, size of critical pores are presented in Fig. 13 using Gumbel's reduced variate. In $P_1\_650°C$ and $P_1\_920°C$ specimens, fatigue cracks initiated either on internal spherical blowhole pores which size range from 21 to 40 µm or on internal lack of fusion pores which size range from 76 to 200 µm (Fig. 12.a–b). One can see in Fig. 11 a drop of fatigue life for those grades when crack initiated on lack of fusion pores. The standard deviation associated with a log-normal distribution of stresses at $10^7$ cycles is 20 MPa (resp. 16 MPa) for $P_1\_650°C$ (resp. $P_1\_920°C$) grade. In $P_2\_920°C$ samples, fatigue cracks initiated on large keyhole pores (90 to 156 µm) or on lack of fusion pores (249 and 644 µm) (Fig. 12.c–d). Although lack of fusion pores are much larger, types of critical pore seem not to affect fatigue life of $P_2\_920°C$ specimens (Fig. 11). Due to the high density of pores in $P_2\_920°C$ samples, $d_{surface}$ is always lower than 500 µm and half of initiations can be considered as subsurface ones for which $\sqrt{Area_{eff}} > d_{surface}$. The largest critical defect ($\sqrt{Area_{eff}} = 644$ µm) was a group of several interacting lack of fusion pores as defined in $\sqrt{Area_{eff}}$ method (Fig. 12.c). On fracture surfaces of $P_1\_1020°C$ samples, microstructural facets are always visible and no pore are visible in 9 out of 10 specimens (Fig. 12.e). Largest facets are as large as grains ($\approx 200$ µm). $\alpha + \beta$ lamellae are visible on these facets. For one $P_1\_1020°C$ specimen, a 12 µm spherical pore within a facet is present on fracture surface (Fig. 12.f). For all $P_0\_920°C$ specimens, SEM with a resolution of 0.1 µm was used for fractographic analysis. No pore nor facets are visible on fracture surface (Fig. 12.g). This means that pores were effectively eliminated during the 2000 bar HIP process. Furthermore, the two $P_0\_920°C$ the two specimens that had the lowest fatigue life were associated with a
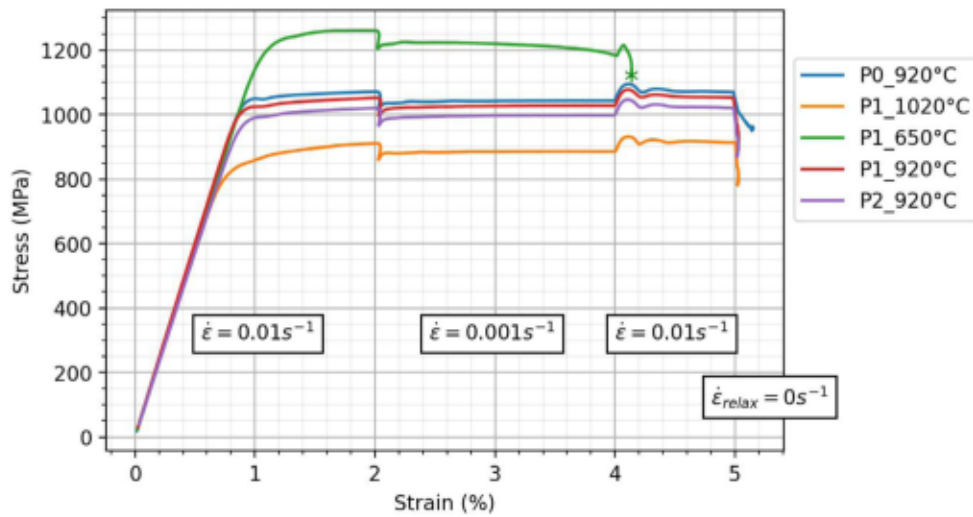
**Fig. 10.** Stress–train curves of tensile tests. Strain rate was $10^{-2}$ s$^{-1}$ for strain 0%–2% and 4%–5% and strain rate was $10^{-3}$ s$^{-1}$ for strain 2%–4%. Strain was maintain at 5% for 5 min for relaxation testing. Sample $P_1$_650°C broke outside the gauge of extensometer before relaxation step.
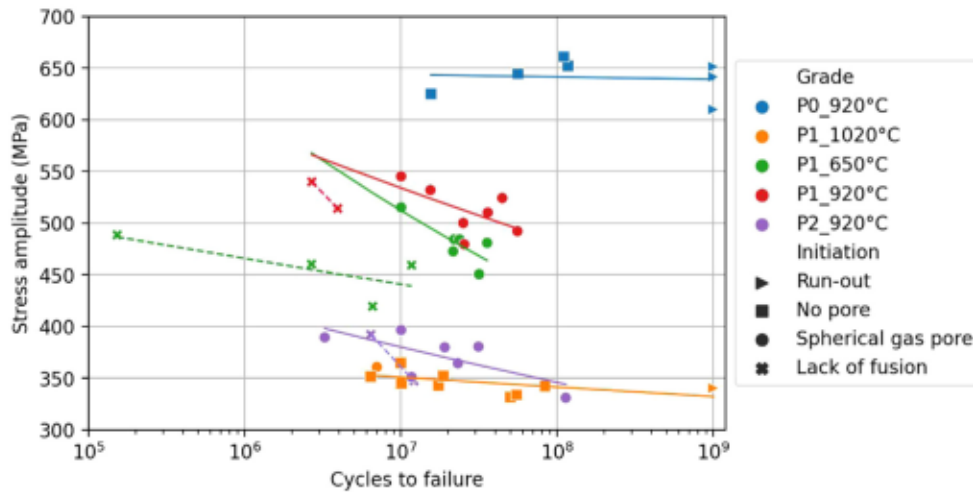


**Fig. 11.** SN curves obtained using ultrasonic fatigue machine. Results are presented according to material grade and type of defect at fatigue crack initiation. Mean curves corresponds to best fitted power law for samples from the same grade. For $P_1$_650°C, $P_1$_920°C and $P_2$_920°C grades, two power laws were calculated according to the type of pore at fatigue crack initiation.

surface crack initiation whereas it was internal for the others. In this study, for all specimens, a dark area, also named fine granular area, was observed using optical microscopy near fatigue crack initiation zone. Its size was 150–300 μm for all specimens except for $P_1$_1020°C specimens in which it was close to 1000 μm.

## 4. Discussion

### 4.1. Process variability and effect of porosity

Although the same machine and powder batch were used, significant process variability can be found between printing batches. As mentioned earlier, two types of critical defect were observed: spherical gas pores and lack of fusion pores. Specimens that initiated from lack of fusion pores came from two out of the five printing batchs. One $P_1$_650°C from a flawed batch was scanned using microtomography and several large and flat pores (i.e. lack of fusion pores) were detected. These pores were located at close vertical coordinates meaning that a problem appeared during LPBF process at this layer. No special event was detected in the manufacturing data apart from an early filter clogging. In this study, lack of fusion pores visible on fractographic

images are relatively flat. Their size along printing direction is small compared to the ones along the two horizontal directions. However, as they are not elongated in one horizontal direction, they do not correspond to unmelted area in between laser tracks (Figs. 12 and 13). They seems to be related either to local lack of powder possibly due to droplet fallen on powder bed or to instantaneous insufficient laser energy. As explained in [13], droplets and nanocondensates present in the vapor plume can reduce the laser energy brought to the powder and cause lack of fusion pores. However, $P_0$_920°C samples from flawed batches were associated with a microstructure-induced fracture. Two $P_0$_920°C samples from flawed batches were also scanned. No pore was detected within tomographic data nor in fractographic analysis meaning that pores were effectively sealed by HIP process. Overall, VHCF fatigue testing results clearly discriminated samples containing lack of fusion pores although process data could not predict their formation. A possible practice when printing structural parts using LPBF, would be to print one or two ultrasonic fatigue test pieces within the same batch in order to validate the batch integrity.

In Fig. 13, distribution of critical pore is not linear in Gumbel's space whereas the distribution obtained using microtomography and block maxima method is linear (Fig. 9). The first one is not linear because
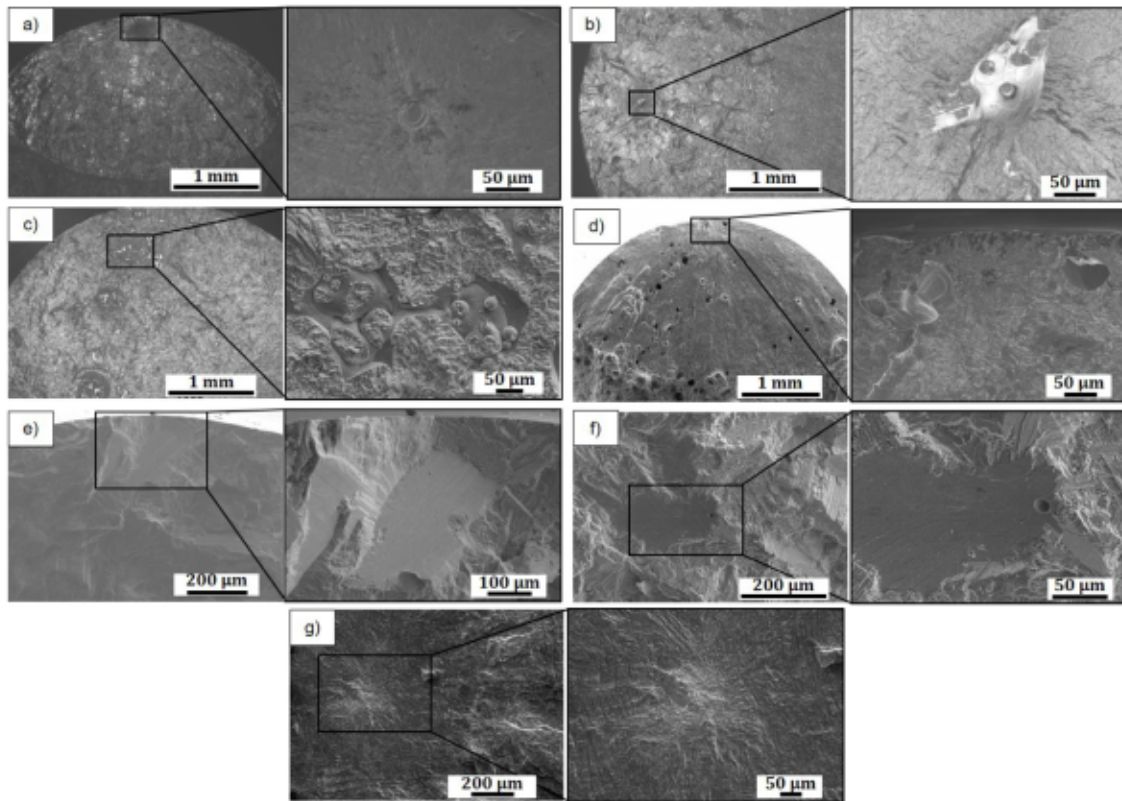
**Fig. 12.** Optical and scanning electronic micrographs of fracture surfaces with different types of crack initiation. (a) Initiation on a spherical gas pore in a $P_1\_650°C$ specimen. (b) Initiation on a lack of fusion pore in a $P_1\_650°C$ specimen. (c) Initiation on a group of interacting lack of fusion pores in a $P_2\_920°C$ specimen. (d) Initiation on a keyhole pore in a $P_2\_920°C$ specimen. (e) Initiation with large microstructural facets in $P_1\_1020°C$ specimen. (f) Initiation with both large microstructural facets and a spherical gas pore in a $P_1\_1020°C$ specimen. (g) Initiation without pore nor large microstructural facets in a $P_0\_920°C$ specimen.
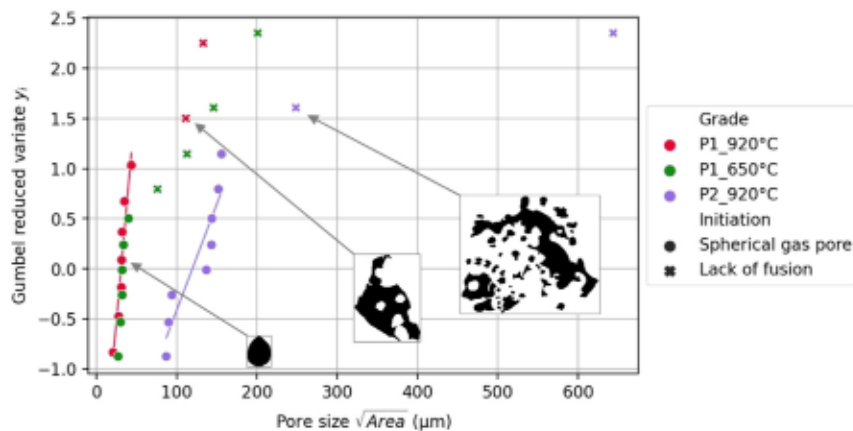


**Fig. 13.** Gumbel distribution of the size of critical pores. Results are presented according to material grade and type of pore at fatigue crack initiation. Linear trends of the distribution for spherical gas pore are represented. Some representative shape of critical defect are represented.

two types of pores with very different size are considered. The second distribution is linear even when lack of fusion pores were present in the part. Indeed, as lack of fusion pores are relatively flat, their effective size $\sqrt{Area_{eff}}$ is much larger than $\sqrt[3]{Volume}$.

The effect of pores on the fatigue strength can be analyzed using Kitagawa–Takahashi (KT) diagram [4]. In this diagram, the plotted models should discriminate the finite and infinite fatigue life domains. Fig. 14 shows the KT diagram with data for specimens from the grades with a microstructure obtained at 920°C. In this diagram, the size of critical defect is defined as $\sqrt{Area_{eff}}$ when initiation was porosity-induced. For visualization purpose, size of defect was set to 1 μm for $P_0\_920°C$ specimens. In Fig. 14, the stress amplitude is the equivalent stress amplitude at $10^7$ cycle. It is obtained using fitted power law calculated for samples with the same grade and the same type of pore at initiation. For each sample the equivalent stress is the stress where the respective mean curve, shifted so that it passes through the considered point, cross $10^7$ cycle. The distinction according to both the grade and the type of pore at initiation allows take into account the bi-modal aspect of the SN curves of these grades (Fig. 11). Three models are represented in Fig. 14: the original KT's model, El-Haddad's model [42] and Murakami's model [5]. The original KT diagram considers two fracture modes. For high stresses and low defect size, fatigue limit corresponds to the one of the defect-free material $\sigma_{a,lim}$. For lower stresses and defect size larger than the critical size,
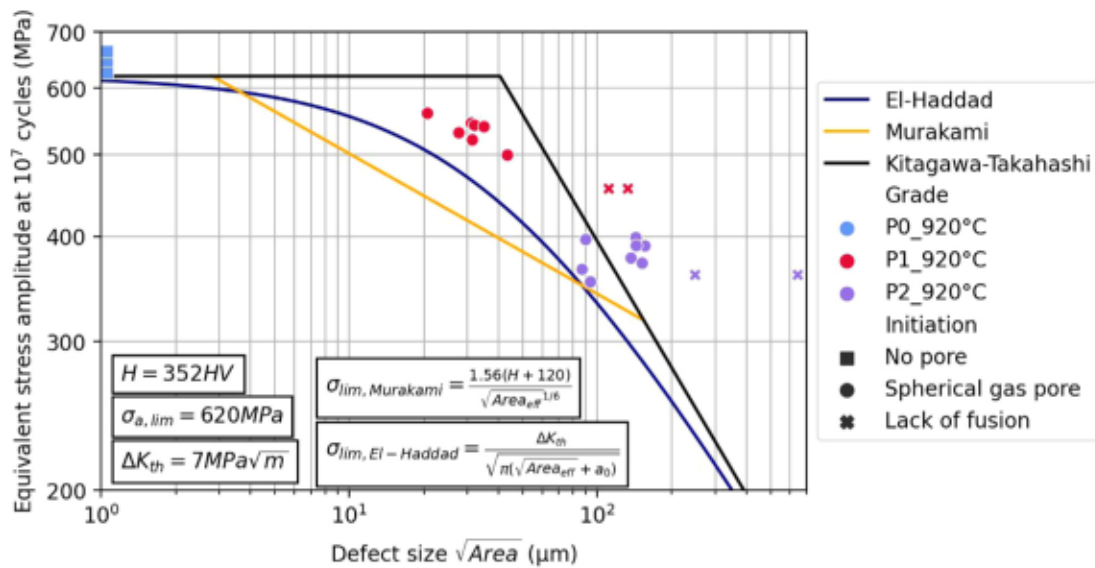
**Fig. 14.** Kitagawa–Takahashi diagram representing the critical defect size $\sqrt{Area_{eff}}$ and the equivalent stress amplitude at $10^7$ cycles for grades with a microstructure obtained at 920°C. El-Haddad's, Murakami's and Kitagawa–Takahashi's models are represented. Murakami's and Kitagawa–Takahashi's models are calculated with factors corresponding to internal crack initiation.

fatigue limit ensues from fatigue long crack propagation threshold. El-Haddad's and Murakami's models are based on KT's one and differ for defect size close to the critical defect size for which short-crack effects cause failure in the safe domain of KT's model. Indeed, short-crack can propagate for stress intensity factors lower than threshold stress intensity factor for long crack propagation. Short-crack effects regroup several phenomena, including crack arrest or crack closure. Recently, the fatigue crack growth model proposed in [43] highlighted the impact of crack closure effects when defect size is close to critical defect size for LPBF–Ti–6Al–4V. El-Haddad's model accounts for short-crack effects by adding a fictive length to the real defect size. Murakami's model corresponds to a short crack propagation threshold based on the hardness of the material. In this study, fatigue limit of the defect-free material was set to $\sigma_{a,lim} = 620$ MPa which corresponds to the fatigue limit of $P_0$_920°C grade. The three models take into account the threshold stress intensity factor for long crack propagation $\Delta K_{th}$. Experimental values of $\Delta K_{th}$ ranging from 3.48 to 4.6 MPa.$\sqrt{m}$ were determined for a load ratio $R = 0.1$ [14,44,45]. Using Walker's equation, Leuders et al. [45] calculated values of $\Delta K_{th}$ ranging from 7.8 to 8.5 MPa.$\sqrt{m}$ for $R = -1$. $\Delta K_{th}$ was here set to 7 MPa.$\sqrt{m}$ leading to a critical defect size: $a_0 = \frac{1}{\pi}(\frac{\Delta K_{th}}{Y\sigma_{a,lim}})^2 = 41$ μm, with $Y = 0.5$ for internal defects. In this study, size of spherical gas pore was often close to the critical defect size for which short crack effects become predominant. Therefore, El-Haddad and Murakami models better represent our data.

### 4.2. Effect of the microstructure

Fig. 15 shows the effect of thermal treatment on microhardness, fatigue strength and grain size. Fatigue strength and hardness values are the ones of $P_1$ grades. Error bars on microhardness curve correspond to the standard deviation over the 10 microhardness measurements performed on each grade. Mean fatigue strength is the stress at $10^7$ cycles of the fitted power law for samples of the grade that do not initiate on lack of fusion pore (Fig. 11). On Fig. 15, error bars on fatigue strength curve correspond to the standard deviation associated with a lognormal dispersion around fitted power laws. Fatigue strength does not vary monotonically with hardness or yield stress as generally observed [5]. According to hardness measurement, $P_1$_650°C grade should have an higher fatigue strength than $P_1$_920°C. This cannot be explained by the size of critical defect as mean size of critical spherical gas pore was 32 μm for both grades. The relatively low

fatigue resistance of $P_1$_650°C grade could be related to martensitic $\alpha'$ present in this grade and not in $P_1$_920°C grade [39]. Indeed, $\alpha'$ phase is more brittle than $\alpha$-phase and $P_1$_650°C specimen used for tensile test did not reach 5% of uniform strain. Moreover, residual stresses can cause this result as they are not fully relaxed in $P_1$_650°C specimens [15] whereas they are in $P_1$_920°C ones [14]. Finally, Kumar and Ramamurty [46] and Tarik Hasib et al. [8] investigated the fatigue crack growth of LPBF Ti–Al–4V followed by a sub $\beta$-transus treatment. They demonstrated that the $\alpha$-lamellae size controls the near threshold fatigue crack growth, this one increases with increasing $\alpha$-lamellae size. Consequently, the near threshold fatigue crack growth is probably lower for $P_1$_650°C than for $P_1$_920°C as the $\alpha$-lamellae is 0.4 μm and 2.2 μm, respectively. Additionally in 920°C the higher fraction of $\beta$-phase should promote crack deflection resulting in an increase of the fatigue crack growth threshold [46]. Overall, an optimal temperature for post-treatment exist as a results of the competition between $\Delta K_{th}$ increase through grain coarsening and yield stress reduction for higher treatment temperature. This optimal temperature should be close to 920°C. In $P_1$_1020°C grade, width of lamellae was smaller than pores whereas grain width was larger. Microstructural facets as large as grains are visible on $P_1$_1020°C fracture surface. Therefore in 1020°C microstructure, lamellar colonies in which all aligned $\alpha$-lamellae have the same crystallographic orientation are the main microstructural barrier to fatigue crack and $\beta$-lamellae within colonies seem not to be a strong microstructural barrier. This is in accordance with the results from [46,47] in which crack path was deflected around lamellar colonies.

### 4.3. Transition from porosity-induced to microstructure-induced fatigue crack initiation

In order to analyze the transition from porosity-induced to microstructure-induced fatigue crack initiation, a grain width – pore size map was developed (Fig. 16). One should note that the location and shape of critical defect should not affect this map. Indeed, for almost all tested specimens, fatigue crack initiation was internal and no correlation between the type (porosity- or microstructure-induced) of fatigue crack initiation and its location was found. Concerning the shape, points associated with the critical lack of fusion pores correspond to the largest pores whose data are far from transition line in Fig. 16. As their uneven shape and their large size both favor crack initiation,
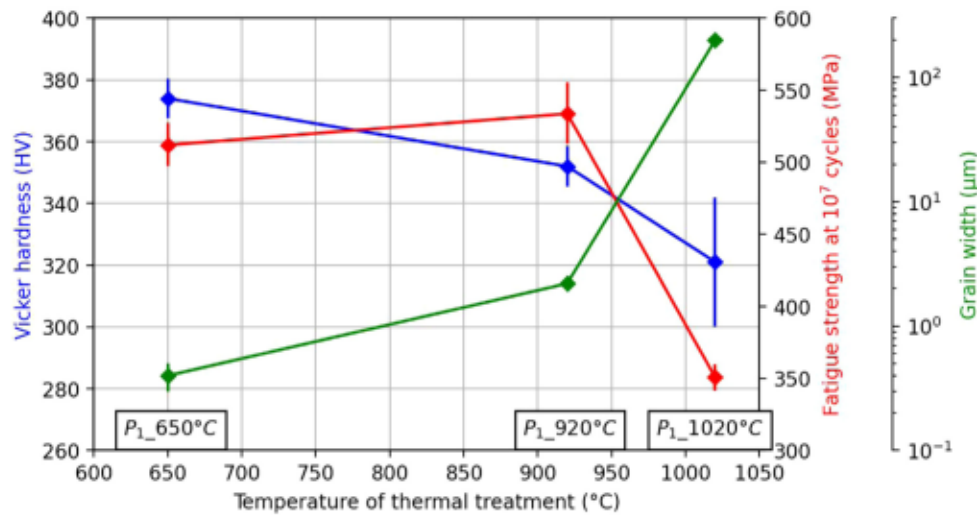
**Fig. 15.** Effect of temperature of thermal treatment on the microhardness, the grain size and the fatigue strength. Fatigue strength values are the ones of grades with the same porosity level $P_i$ and without considering specimens that initiated on lack of fusion pores.
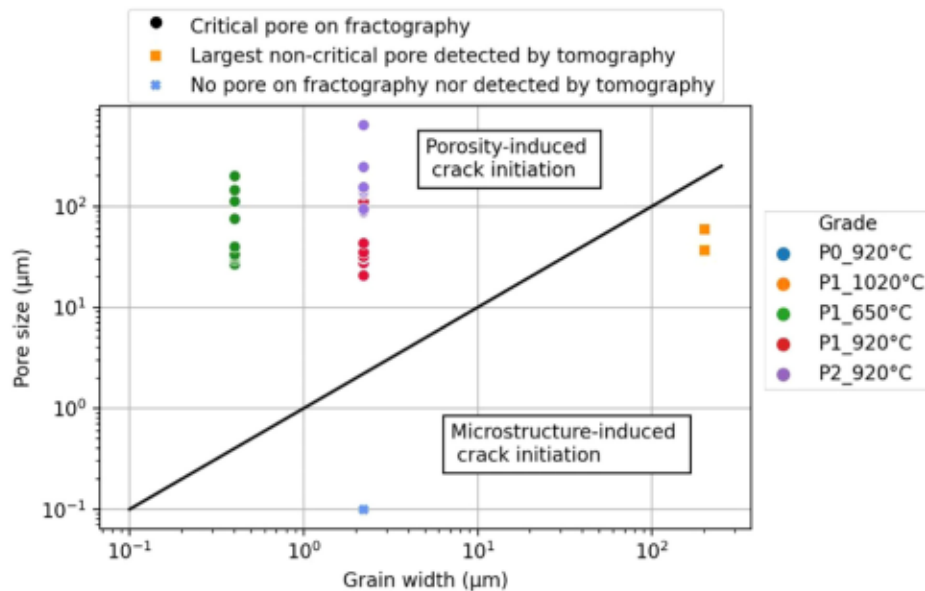


**Fig. 16.** Relationship between the width of grain, the size of pore and the resulting type of fatigue crack initiation. Pore size corresponds either to the size of critical pore, or the size of non critical pore detected by tomography in $P_1$_1020°C specimens (Table 2) or the resolution of SEM used during fractographic analysis when no pore was detected.

it is not possible to separate the shape and size effects in the case of lack of fusion pores. However, the shape effect is included in the size effect as the considered size for lack of fusion pores is the surrounding convex area ($\sqrt{Area_{eff}}$ method). The case of subsurface defects is also considered with this method as in this case $Area_{eff}$ includes the ligament between the surface and the pore. Furthermore, shapes of critical spherical gas pores are similar and this defect population is also present in $P_1$_1020°C grade (Fig. 9) although it is not critical in 1020°C microstructure. Within the map on Fig. 16, the solid line separates two areas. At the top left, for a given specimen pore size is larger than grain width, whereas it is smaller at the bottom right. Plotted pore size corresponds either to the size of critical pore visible on fracture surface or to the largest pore size detected by tomography within specimen associated with a microstructure-induced crack initiation (Table 2). For visualization purpose, $P_0$_920°C specimens in which no pore was detected on fracture surface were plotted with a pore size of 0.1 μm, corresponding to the resolution of SEM used during fractographic analysis. The microstructure size corresponds to size of the critical grain visible on fracture surface or to the mean grain width

in Table 3 for pore-induced crack initiation specimens. One should note the limited dispersion of both grain size (Table 3) and size of critical gas pore in $P_1$ specimens (21 to 40 μm). Map in Fig. 16 shows a clear separation between data associated with a porosity-induced or microstructure-induced fatigue crack initiation. A correlation between the type of the critical defect and its size is clearly highlighted. Whatever critical defect (grain or pore), it seems that the largest one controls crack initiation. It should be noted that highly-stressed volume in ultrasonic fatigue specimen is large enough so that several pores larger than 10 μm are always present within this volume (pore density in Table 2). This volume is also large as compared to the size of grain whatever the material grade. Volume effect should therefore not affect the map on Fig. 16. Vincent et al. [48], obtained similar results on pure ARMCO iron in which transition from grain to porosity-induced crack initiation appeared when pores became larger than grains. It is worth noticing that ARMCO iron is a single-phase pure material having a simple microstructure. In the present case, LPBF–Ti–6Al–4V specimens exhibit multiple phases with various amount and spatial arrangement. In the present study, the size of critical or largest pores

and the size of microstructure for the same specimen differ from about one order of magnitude. Investigating specimen exhibiting lower differences between these two sizes is necessary to analyze more deeply the transition between grain and porosity-induced crack initiation and the role of other microstructural features on crack initiation site. For close microstructures, the transition from grain to porosity-induced crack initiation is well described by Kitagawa–Takahashi's approach and Murakami's equation in HCF [5,47,49]. It is shown here that it also applies in the VHCF regime despite that internal defects such as pores are known to play a first-order role in crack initiation [27,31].

## 5. Conclusions

The aim of this study was to examine how variations of porosity and microstructure affect the VHCF properties of LPBF–Ti–6Al–4V. The main findings of this work were:

- LPBF specimens with a reproducible target porosity were obtained by adjusting the laser scan strategy. LPBF specimens with a target microstructure without any changes in porosity were obtained by adjusting subsequent heat treatments. Overall, the developed processing routes allow to separately investigate microstructure and porosity effects on the properties of LPBF–Ti–6Al–4V.
- Fast fatigue testing using ultrasonic fatigue was sensitive to both porosity and microstructure variations making it suitable for the optimization of AM parameter and thermomechanical post-treatments. Moreover, as process variability is limited within each printing batch, few specimens can be tested using ultrasonic fatigue machine to monitor batch quality.
- Whatever the critical defect (pore or grain) fatigue crack initiation was almost always internal.
- When the size of critical or largest pores and the size of microstructure differ from about one order of magnitude, a correlation between the type of the critical defect and its size was clearly highlighted. The size of the critical defect (pore or grain) has a first order effect on fatigue crack initiation compared to the type of microstructural barriers, present phases or the shape of defects.
- For 920°C heat-treated specimens, the transition from grain to porosity-induced crack initiation is well described by Kitagawa–Takahashi's approach and Murakami's equation.

## CRediT authorship contribution statement

**Grégoire Brot:** Methodology, Formal analysis, Investigation, Writing – original draft, Visualization. **Imade Koutiri:** Conceptualization, Methodology, Writing – review & editing. **Vincent Bonnand:** Conceptualization, Methodology, Writing – review & editing, Funding acquisition. **Véronique Favier:** Conceptualization, Methodology, Writing – review & editing. **Corinne Dupuy:** Methodology, Investigation. **Nicolas Ranc:** Conceptualization, Writing – review & editing. **Patrick Aimedieu:** Formal analysis, Investigation, Writing – review & editing. **Fabien Lefebvre:** Conceptualization, Writing – review & editing, Funding acquisition. **Robin Hauteville:** Writing – review & editing.

## Declaration of competing interest

The authors declare that they have no known competing financial interests or personal relationships that could have appeared to influence the work reported in this paper.

## Data availability

Data will be made available on request

## References

[1] Kasperovich G, Hausmann J. Improvement of fatigue resistance and ductility of TiAl6V4 processed by selective laser melting. J Mater Process Technol 2015;220:202–14. http://dx.doi.org/10.1016/j.jmatprotec.2015.01.025, URL https://linkinghub.elsevier.com/retrieve/pii/S0924013615000278.

[2] Kumar P, Prakash O, Ramamurty U. Micro-and meso-structures and their influence on mechanical properties of selectively laser melted Ti–6Al–4V. Acta Mater 2018;154:246–60. http://dx.doi.org/10.1016/j.actamat.2018.05.044, URL https://www.sciencedirect.com/science/article/pii/S1359645418304117.

[3] Le V-D, Pessard E, Morel F, Edy F. Interpretation of the fatigue anisotropy of additively manufactured TA6V alloys via a fracture mechanics approach. Eng Fract Mech 2019;214:410–26. http://dx.doi.org/10.1016/j.engfracmech.2019.03.048, URL https://linkinghub.elsevier.com/retrieve/pii/S0013794418311664.

[4] Kitagawa H, Takahashi S. Applicability of fracture mechanics to very small cracks or the cracks in the early stage. Int Conf Mech Behav Mater 1976;2nd:627–31.

[5] Murakami Y. Metal fatigue: effects of small defects and nonmetallic inclusions. San Diego: Elsevier Science Publishing Co Inc; 2019, OCLC: 1096516382.

[6] Spears T, Gold S. In-process sensing in selective laser melting (SLM) additive manufacturing. Integr Mater Manuf Innov 2016;5. http://dx.doi.org/10.1186/s40192-016-0045-4.

[7] Shipley H, McDonnell D, Culleton M, Coull R, Lupoi R, O'Donnell G, et al. Optimisation of process parameters to address fundamental challenges during selective laser melting of Ti–6Al–4V: A review. Int J Mach Tools Manuf 2018;128:1–20. http://dx.doi.org/10.1016/j.ijmachtools.2018.01.003, URL https://linkinghub.elsevier.com/retrieve/pii/S0890695518300233.

[8] Tarik Hasib M, Ostergaard HE, Li X, Kruzic JJ. Fatigue crack growth behavior of laser powder bed fusion additive manufactured Ti–6Al–4V: Roles of post heat treatment and build orientation. Int J Fatigue 2021;142:105955. http://dx.doi.org/10.1016/j.ijfatigue.2020.105955, URL https://linkinghub.elsevier.com/retrieve/pii/S0142112320304874.

[9] Vrancken B, Thijs L, Kruth J-P, Van Humbeeck J. Heat treatment of Ti6Al4V produced by selective laser melting: Microstructure and mechanical properties. J Alloys Compd 2012;541:177–85. http://dx.doi.org/10.1016/j.jallcom.2012.07.022, URL https://linkinghub.elsevier.com/retrieve/pii/S0925838812011826.

[10] Simonelli M, Tse YY, Tuck C. The formation of alpha + beta microstructure in as-fabricated selective laser melting of Ti–6Al–4V. J Mater Res 2014;29(17):2028–35. http://dx.doi.org/10.1557/jmr.2014.166, URL http://link.springer.com/10.1557/jmr.2014.166.

[11] Xu W, Brandt M, Sun S, Elambasseril J, Liu Q, Latham K, et al. Additive manufacturing of strong and ductile Ti–6Al–4V by selective laser melting via in situ martensite decomposition. Acta Mater 2015;85:74–84. http://dx.doi.org/10.1016/j.actamat.2014.11.028, URL https://www.sciencedirect.com/science/article/pii/S1359645414008817.

[12] Yang J, Yu H, Yin J, Gao M, Wang Z, Zeng X. Formation and control of martensite in Ti–6Al–4V alloy produced by selective laser melting. Mater Des 2016;108:308–18. http://dx.doi.org/10.1016/j.matdes.2016.06.117, URL https://linkinghub.elsevier.com/retrieve/pii/S0264127516308796.

[13] de Terris T, Andreau O, Peyre P, Adamski F, Koutiri I, Gorny C, et al. Optimization and comparison of porosity rate measurement methods of selective laser melted metallic parts. Addit Manuf 2019;28:802–13. http://dx.doi.org/10.1016/j.addma.2019.05.035, URL https://linkinghub.elsevier.com/retrieve/pii/S2214860418307723.

[14] Leuders S, Thöne M, Riemer A, Niendorf T, Tröster T, Richard HA, et al. On the mechanical behaviour of titanium alloy TiAl6V4 manufactured by selective laser melting: Fatigue resistance and crack growth performance. Int J Fatigue 2013;48:300–7. http://dx.doi.org/10.1016/j.ijfatigue.2012.11.011, URL https://linkinghub.elsevier.com/retrieve/pii/S014211231200343X.

[15] Syed AK, Ahmad B, Guo H, Machry T, Eatock D, Meyer J, et al. An experimental study of residual stress and direction-dependence of fatigue crack growth behaviour in as-built and stress-relieved selective-laser-melted Ti6Al4V. Mater Sci Eng A 2019;755:246–57. http://dx.doi.org/10.1016/j.msea.2019.04.023, URL https://linkinghub.elsevier.com/retrieve/pii/S0921509319304691.

[16] Kaschel FR, Vijayaraghavan RK, McNally PJ, Dowling DP, Celikin M. In-situ XRD study on the effects of stress relaxation and phase transformation heat treatments on mechanical and microstructural behaviour of additively manufactured Ti–6Al–4V. Mater Sci Eng A 2021;819:141534. http://dx.doi.org/10.1016/j.msea.2021.141534, URL https://www.sciencedirect.com/science/article/pii/S0921509321008030.

[17] Etesami SA, Fotovvati B, Asadi E. Heat treatment of Ti–6Al–4V alloy manufactured by laser-based powder-bed fusion: Process, microstructures, and mechanical properties correlations. J Alloys Compd 2022;895:162618. http://dx.doi.org/10.1016/j.jallcom.2021.162618, URL https://www.sciencedirect.com/science/article/pii/S0925838821040287.

[18] Vilaro T, Colin C, Bartout JD. As-fabricated and heat-treated microstructures of the Ti–6Al–4V alloy processed by selective laser melting. Metall Mater Trans A 2011;42(10):3190–9. http://dx.doi.org/10.1007/s11661-011-0731-y, URL http://link.springer.com/10.1007/s11661-011-0731-y.

[19] Ter Haar GM, Becker T, Blaine DC. Influence of heat treatments on the microstructure and tensile behavior of selective laser melting-produced Ti–6Al–4V parts. S Afr J Ind Eng 2016;27(3). http://dx.doi.org/10.7166/27-3-1663, URL http://sajie.journals.ac.za/pub/article/view/1663.

[20] Cecchel S, Ferrario D, Cornacchia G, Gelfi M. Development of heat treatments for selective laser melting Ti6Al4V alloy: Effect on microstructure, mechanical properties, and corrosion resistance. Adv Eng Mater 2020;22(8). http://dx.doi.org/10.1002/adem.202000359.

[21] Moran TP, Carrion PE, Lee S, Shamsaei N, Phan N, Warner DH. Hot isostatic pressing for fatigue critical additively manufactured Ti–6Al–4V. Materials 2022;15(6):2051. http://dx.doi.org/10.3390/ma15062051, URL https://www.mdpi.com/1996-1944/15/6/2051.

[22] Zhang D, Wang L, Zhang H, Maldar A, Zhu G, Chen W, et al. Effect of heat treatment on the tensile behavior of selective laser melted Ti–6Al–4V by in situ X-ray characterization. Acta Mater 2020;189:93–104. http://dx.doi.org/10.1016/j.actamat.2020.03.003, URL https://www.sciencedirect.com/science/article/pii/S1359645420301804.

[23] Bathias C, Paris PC. Gigacycle fatigue in mechanical practice. Marcel Dekker; 2005.

[24] Li P, Warner DH, Fatemi A, Phan N. Critical assessment of the fatigue performance of additively manufactured Ti–6Al–4V and perspective for future research. Int J Fatigue 2016;85:130–43. http://dx.doi.org/10.1016/j.ijfatigue.2015.12.003, URL https://linkinghub.elsevier.com/retrieve/pii/S0142112315004399.

[25] Leuders S, Lieneke T, Lammers S, Tröster T, Niendorf T. On the fatigue properties of metals manufactured by selective laser melting – the role of ductility. J Mater Res 2014;29(17):1911–9. http://dx.doi.org/10.1557/jmr.2014.157, URL http://link.springer.com/10.1557/jmr.2014.157.

[26] da Costa PR, Sardinha M, Reis L, Freitas M, Fonte M. Ultrasonic fatigue testing in as-built and polished Ti6Al4V alloy manufactured by SLM. Forces Mech 2021;100024. http://dx.doi.org/10.1016/j.finmec.2021.100024, URL https://www.sciencedirect.com/science/article/pii/S2666359721000159.

[27] Günther J, Krewerth D, Lippmann T, Leuders S, Tröster T, Weidner A, et al. Fatigue life of additively manufactured Ti–6Al–4V in the very high cycle fatigue regime. Int J Fatigue 2017;94:236–45. http://dx.doi.org/10.1016/j.ijfatigue.2016.05.018, URL https://linkinghub.elsevier.com/retrieve/pii/S0142112316301207.

[28] Du L, Pan X, Qian G, Zheng L, Hong Y. Crack initiation mechanisms under two stress ratios up to very-high-cycle fatigue regime for a selective laser melted Ti–6Al–4V. Int J Fatigue 2021;149:106294. http://dx.doi.org/10.1016/j.ijfatigue.2021.106294, URL https://www.sciencedirect.com/science/article/pii/S0142112321001547.

[29] Tridello A, Fiocchi J, Biffi CA, Chiandussi G, Rossetto M, Tuissi A, et al. VHCF response of heat-treated SLM Ti6Al4V Gaussian specimens with large loaded volume. Procedia Struct Integr 2019;18:314–21. http://dx.doi.org/10.1016/j.prostr.2019.08.171, URL https://linkinghub.elsevier.com/retrieve/pii/S2452321619303816.

[30] Wycisk E, Siddique S, Herzog D, Walther F, Emmelmann C. Fatigue performance of laser additive manufactured Ti–6Al–4V in very high cycle fatigue regime up to 109 cycles. Front Mater 2015;2. http://dx.doi.org/10.3389/fmats.2015.00072, URL http://journal.frontiersin.org/Article/10.3389/fmats.2015.00072/abstract.

[31] Qian G, Li Y, Paolino DS, Tridello A, Berto F, Hong Y. Very-high-cycle fatigue behavior of Ti–6Al–4V manufactured by selective laser melting: Effect of build orientation. Int J Fatigue 2020;136:105628. http://dx.doi.org/10.1016/j.ijfatigue.2020.105628.

[32] Morrissey R, Nicholas T. Staircase testing of a titanium alloy in the gigacycle regime. In: Third international conference on very high cycle fatigue, 28, (11):2006, p. 1577–82. http://dx.doi.org/10.1016/j.ijfatigue.2005.10.007, URL http://www.sciencedirect.com/science/article/pii/S0142112306000922.

[33] Hu YN, Wu SC, Wu ZK, Zhong XL, Ahmed S, Karabal S, et al. A new approach to correlate the defect population with the fatigue life of selective laser melted Ti–6Al–4V alloy. Int J Fatigue 2020;136:105584. http://dx.doi.org/10.1016/j.ijfatigue.2020.105584, URL https://linkinghub.elsevier.com/retrieve/pii/S0142112320301158.

[34] Chi W, Li G, Wang W, Sun C. Interior initiation and early growth of very high cycle fatigue crack in an additively manufactured Ti-alloy. Int J Fatigue 2022;160:106862. http://dx.doi.org/10.1016/j.ijfatigue.2022.106862, URL https://www.sciencedirect.com/science/article/pii/S0142112322001372.

[35] Mughrabi H. On 'multi-stage' fatigue life diagrams and the relevant life-controlling mechanisms in ultrahigh-cycle fatigue. Fatigue Fract Eng Mater Struct 2002;25(8):755–64. http://dx.doi.org/10.1046/j.1460-2695.2002.00550.x, URL https://onlinelibrary.wiley.com/doi/abs/10.1046/j.1460-2695.2002.00550.x.

[36] Pessard E, Lavialle M, Laheurte P, Didier P, Brochu M. High-cycle fatigue behavior of a laser powder bed fusion additive manufactured Ti–6Al–4V titanium: Effect of pores and tested volume size. Int J Fatigue 2021;149:106206. http://dx.doi.org/10.1016/j.ijfatigue.2021.106206, URL https://www.sciencedirect.com/science/article/pii/S0142112321000669.

[37] Jacquemain V, Ranc N, Cheuleu C, Michel V, Favier V, Castelnau O, et al. Estimation of stress in specimens loaded with ultrasonic fatigue machines. Int J Fatigue 2021;153:106474. http://dx.doi.org/10.1016/j.ijfatigue.2021.106474, URL https://www.sciencedirect.com/science/article/pii/S0142112321003327.

[38] Masuo H, Tanaka Y, Morokoshi S, Yagura H, Uchida T, Yamamoto Y, et al. Influence of defects, surface roughness and HIP on the fatigue strength of Ti–6Al–4V manufactured by additive manufacturing. Int J Fatigue 2018;117:163–79. http://dx.doi.org/10.1016/j.ijfatigue.2018.07.020, URL https://linkinghub.elsevier.com/retrieve/pii/S0142112318303050.

[39] Kaschel FR, Vijayaraghavan RK, Shmeliov A, McCarthy EK, Canavan M, McNally PJ, et al. Mechanism of stress relaxation and phase transformation in additively manufactured Ti–6Al–4V via in situ high temperature XRD and TEM analyses. Acta Mater 2020;188:720–32. http://dx.doi.org/10.1016/j.actamat.2020.02.056, URL https://www.sciencedirect.com/science/article/pii/S1359645420301695.

[40] Gil Mur FX, Rodríguez D, Planell JA. Influence of tempering temperature and time on the alpha'-Ti–6Al–4V martensite. J Alloys Compd 1996;234(2):287–9. http://dx.doi.org/10.1016/0925-8388(95)02057-8, URL https://www.sciencedirect.com/science/article/pii/0925838895020578.

[41] Heinz S, Balle F, Wagner G, Eifler D. Analysis of fatigue properties and failure mechanisms of Ti6Al4V in the very high cycle fatigue regime using ultrasonic technology and 3D laser scanning vibrometry. In: Ultrasonic fatigue of advanced materials, 53, (8):2013, p. 1433–40. http://dx.doi.org/10.1016/j.ultras.2013.03.002, URL http://www.sciencedirect.com/science/article/pii/S0041624X13000644.

[42] El Haddad MH, Topper TH, Smith KN. Prediction of non propagating cracks. Eng Fract Mech 1979;11(3):573–84. http://dx.doi.org/10.1016/0013-7944(79)90081-X, URL https://www.sciencedirect.com/science/article/pii/001379447990081X.

[43] Macallister N, Becker TH. Fatigue life estimation of additively manufactured Ti–6Al–4V: Sensitivity, scatter and defect description in damage-tolerant models. Acta Mater 2022;237:118189. http://dx.doi.org/10.1016/j.actamat.2022.118189, URL https://www.sciencedirect.com/science/article/pii/S1359645422005705.

[44] Wycisk E, Solbach A, Siddique S, Herzog D, Walther F, Emmelmann C. Effects of defects in laser additive manufactured Ti–6Al–4V on fatigue properties. In: 8th international conference on laser assisted net shape engineering, 56, 2014, p. 371–8. http://dx.doi.org/10.1016/j.phpro.2014.08.120, URL http://www.sciencedirect.com/science/article/pii/S187553892140026SX.

[45] Leuders S, Vollmer M, Brenne F, Tröster T, Niendorf T. Fatigue strength prediction for titanium alloy TiAl6V4 manufactured by selective laser melting. Metall Mater Trans A 2015;46(9):3816–23. http://dx.doi.org/10.1007/s11661-015-2864-x, URL http://link.springer.com/10.1007/s11661-015-2864-x.

[46] Kumar P, Ramamurty U. Microstructural optimization through heat treatment for enhancing the fracture toughness and fatigue crack growth resistance of selective laser melted Ti6Al4V alloy. Acta Mater 2019;169:45–59. http://dx.doi.org/10.1016/j.actamat.2019.03.003, URL https://www.sciencedirect.com/science/article/pii/S1359645419301363.

[47] Nalla RK, Ritchie RO, Boyce BL, Campbell JP, Peters JO. Influence of microstructure on high-cycle fatigue of Ti–6Al–4V: Bimodal vs. lamellar structures. Metall Mater Trans A 2002;33(3):899–918. http://dx.doi.org/10.1007/s11661-002-0160-z.

[48] Vincent M, Nadot Y, Nadot-Martin C, Dragon A. Interaction between a surface defect and grain size under high cycle fatigue loading: Experimental approach for Armco iron. Int J Fatigue 2016;87:81–90. http://dx.doi.org/10.1016/j.ijfatigue.2016.01.013, URL https://www.sciencedirect.com/science/article/pii/S0142112316000141.

[49] Rigon D, Meneghetti G. An engineering estimation of fatigue thresholds from a microstructural size and vickers hardness: Application to wrought and additively manufactured metals. Int J Fatigue 2020;139:105796. http://dx.doi.org/10.1016/j.ijfatigue.2020.105796, URL https://www.sciencedirect.com/science/article/pii/S0142112320303273.